World Academy of Science, Engineering and Technology
International Journal of Mechanical and Mechatronics Engineering
Vol:7, No:4, 2013

Finite Element Prediction of Multi-Size Particulate Flow through Two-Dimensional Pump Casing

K. V. Pagalthivarthi, R. J. Visintainer

***Abstract*—**Two-dimensional Eulerian (volume-averaged) continuity and momentum equations governing multi-size slurry flow through pump casings are solved by applying a penalty finite element formulation. The computational strategy validated for multi-phase flow through rectangular channels is adapted to the present study. The flow fields of the carrier, mixture and each solids species, and the concentration field of each species are determined sequentially in an iterative manner. The eddy viscosity field computed using Spalart-Allmaras model for the pure carrier phase is modified for the presence of particles. Streamline upwind Petrov-Galerkin formulation is used for all the momentum equations for the carrier, mixture and each solids species and the concentration field for each species. After ensuring mesh-independence of solutions, results of multi-size particulate flow simulation are presented to bring out the effect of bulk flow rate, average inlet concentration, and inlet particle size distribution. Mono-size computations using (1) the concentration-weighted mean diameter of the slurry and (2) the D50 size of the slurry are also presented for comparison with multi-size results.

***Keywords*—**Eulerian-Eulerian model, Multi-size particulate flow, Penalty finite elements, Pump casing, Spalart-Allmaras.

I. Introduction

CENTRIFUGAL slurry pump casings are often subject to non-uniform wear, leading to premature replacement of expensive hard-to-repair hard cast iron alloy casings due to high localized wear. Such replacement of eroded pump casings increases the unscheduled downtime as well as operational costs of the pipeline system. Thus, finite element computational tools to predict solid-liquid flows and the consequent erosion distribution have been in use since the early eighties [1]-[6]. In these studies, the slurry is characterized by a single particle size (taken as the D50 mesh size) of the slurry. The highlights and limitations of each of these works have been presented by Addie et al. [6].

Most of these studies employ a potential function or stream function formulation to compute the mixture flow field (which is assumed to be affected negligibly by the assumed relatively fine solids). The expected solids velocity at each node is computed writing a balance between the pressure force, gravitational force, inertial force and drag force. The concentration field is governed by a convection-diffusion equation. Since the concentration field and solids velocity field are mutually related, an iterative solution alternating between these two fields is employed. Pagalthivarthi et al. [4] and Visintainer et al. [5] extend these ideas to a quasi-3D model to compute solid-liquid flow field in any specified radial cross section of the pump.

A mixing length based viscous model [6] has been previously developed for mono-size slurry flow simulation in two-dimensional pump casings using the Galerkin finite element method.

The mono-size slurries dealt with in the foregoing discussion often do not adequately represent industrial slurries containing a broad range of particle sizes. To represent them by a single effective particle size is inadequate from the points of view of erosion prediction as well as solids effect on pump performance. A significant improvement could result if the particle size distribution is represented in terms of a specified number of size intervals (called species), each with a representative diameter. Thus the slurry is treated as multi-size particulate mixture carried in a medium. This approach has been effectively implemented in several recent studies involving pipe flow [7], horizontal duct flow [8], and rotating channel flow [9]–[11].

The aim of this study has been to incorporate this multi-size particulate feature in two-dimensional slurry flow prediction through pump casings. Apart from this, following the successful predictions of pipe flow and duct flow of Ravichandra et al. [7] and Pagalthivathi et al. [8], the present study departs in the following significant ways from the previous casing study efforts:

- A concentration-modified Spalart Allmaras (SA) [12], [13] turbulence model is introduced in this study to account for turbulence.
- A penalty finite element algorithm is used to compute the carrier phase and mixture flow fields. The common pressure field is then computed from the mixture flow field using a least squares method. Four-node bilinear interpolation is used for all velocity components, and for the concentration fields.
- Streamline Upwind Petrov-Galerkin (SUPG) Finite element method [14] is introduced to stabilize the finite element computations.
- For six particle size classes considered in this study, the full computational algorithm solves for a total of 22 field variables, *viz*. mixture velocity components and pressure, solids velocity components and solids concentration for each of the six size classes, and the transport equation for the Spalart-Allmaras turbulence model. An overall iterative solution procedure deals with mixture velocity, mixture pressure, solids velocity and solids concentration in the inner iterative loops.
- Wall functions are employed for each of the solid species

K. V. Pagalthivarthi is with GIW Industries Inc., Wrightsboro Road, Georgia, GA – 30813, USA (e-mail: krish18pag@yahoo.com).

R. J. Visintainer is with GIW Industries Inc., Wrightsboro Road, Georgia, GA – 30813, USA.

in a manner similar to that used for single phase flow computations.

II. Computational Domain and Mathematical Model

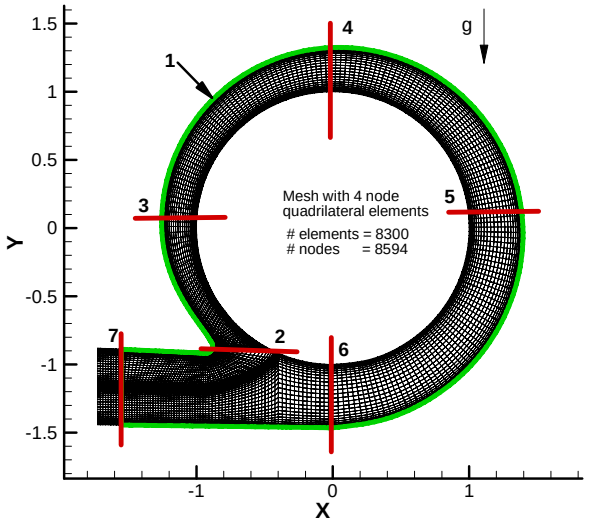

Fig. 1 Computational domain with typical finite element mesh

A pump casing cross-section normal to the pump axis is shown (Fig. 1) with a typical finite element mesh consisting of four-node quadrilateral elements. The two-dimensional computational domain consists of the meshed region between the impeller outlet circumference and the casing peripheral wall. Dense slurry with a broad particle size distribution (represented by N particle size classes, each with a specific mean diameter) enters the flow domain at the impeller exit and leaves the casing through the discharge exit. In order to conveniently apply zero-gradient boundary conditions at the exit, the computational domain is usually extended beyond the physical location of the exit. Given the mean flow conditions (the flow rate and the average concentration of each solids species) at the domain entrance, the problem is to determine the steady (in the mean) flow field of the mixture and each of the particulate species inside the computational domain. The mixture flow rate, Q_m, the inlet volumetric concentration C_{ka} of each of the N species, and the effective head generated, H_0, by the pump are the specified input parameters for a specified casing geometry.

A. Governing Equations

Based on Davidson [15], the mathematical development of the equations governing steady (in the mean), two-dimensional, multi-size slurry flow is presented by Pagalthivarthi et al. [8] and Gupta and Pagalthivarthi [10]. Non-dimensional forms of the equations are obtained as follows: all lengths are divided by the reference length L (the impeller radius in the present study), all velocity components are divided by the reference velocity U_0 (the impeller peripheral speed), and pressure is divided by $\rho_L U_o^2$, ρ_L being the carrier density. Only the final relevant scalar non-dimensional equations are presented in the following.

The mixture continuity equation is given as

$$\frac{\partial}{\partial x}(S_m u_m)+\frac{\partial}{\partial y}(S_m v_m)=0 \tag{1}$$

where S_m is the specific density of the mixture, defined as the ratio of the mixture density (ρ_m) to the carrier liquid density (ρ_L), u_m is the x-component of the mixture velocity and v_m is its y-component. The mixture density and mixture velocity ($\vec{u}_m$) are defined as

$$\rho_m=\sum_{k=1}^{N+1}\rho_k C_k \tag{2}$$

and

$$\vec{u}_m=\frac{\sum_{k=1}^{N+1}\rho_k C_k \vec{u}_k}{\rho_m} \tag{3}$$

where ρ_k, C_k and $\vec{u}_k$ are the density, volumetric concentration and velocity of the k^{th} species ($k = N+1$ stands for the carrier liquid, $k = 1$ to N stand for solids species).

After incorporating the constitutive relationships, the scalar mixture momentum equations are given as

$$\frac{\partial}{\partial x}\left(S_m u_m^2\right)+\frac{\partial}{\partial y}\left(S_m u_m v_m\right)=-\frac{\partial p}{\partial x}+\frac{\partial}{\partial x}\left(\frac{\mu_m^*+\mu_{mt}^*}{\text{Re}}\right)\left\{\frac{4}{3}\frac{\partial u_m}{\partial x}-\frac{2}{3}\frac{\partial v_m}{\partial y}\right\}+\frac{\partial}{\partial y}\left(\frac{\mu_m^*+\mu_{mt}^*}{\text{Re}}\right)\left\{\frac{\partial u_m}{\partial y}+\frac{\partial v_m}{\partial x}\right\}, \tag{4}$$

and

$$\frac{\partial}{\partial x}\left(S_m u_m v_m\right)+\frac{\partial}{\partial y}\left(S_m v_m v_m\right)=-\frac{\partial p}{\partial y}+\frac{\partial}{\partial x}\left(\frac{\mu_m^*+\mu_{mt}^*}{\text{Re}}\right)\left\{\frac{\partial u_m}{\partial y}+\frac{\partial v_m}{\partial x}\right\}+\frac{\partial}{\partial y}\left(\frac{\mu_m^*+\mu_{mt}^*}{\text{Re}}\right)\left\{\frac{4}{3}\frac{\partial v_m}{\partial y}-\frac{2}{3}\frac{\partial u_m}{\partial x}\right\}, \tag{5}$$

where $\mu_m^*=\mu_m/\mu_L$, $\mu_{mt}^*=\mu_{mt}/\mu_L$, p is the pressure (assumed equal for the mixture and all the phases), and Re is the flow Reynolds number ($\text{Re}=\frac{\rho_L U_o L}{\mu_L}$), μ_L is the dynamic viscosity of the carrier liquid. The mixture laminar viscosity (μ_m) and turbulent viscosity (μ_{mt}) are derived (following an earlier study by Pagalthivarthi et al. [8]) from the laminar and turbulent viscosities of the pure carrier phase by semi-empirically determined (Roco and Shook [2] and Roco and Balakrishnan [16]) modifications to account for particles.

The turbulent eddy viscosity of the pure carrier phase is computed from the Spalart-Allmaras model [12]. The governing equations for the pure carrier-phase flow can be written in non-dimensional form as

$$\frac{\partial u}{\partial x}+\frac{\partial v}{\partial y}=0, \tag{6}$$

$$u\frac{\partial u}{\partial x}+v\frac{\partial u}{\partial y}=\frac{\partial}{\partial x}\left\{2\frac{1+\mu_r}{\mathrm{Re}}\left(\frac{\partial u}{\partial x}\right)-p\right\}+\frac{\partial}{\partial y}\left\{\frac{1+\mu_r}{\mathrm{Re}}\left(\frac{\partial u}{\partial y}+\frac{\partial v}{\partial x}\right)\right\} \quad (7)$$

and

$$u\frac{\partial v}{\partial x}+v\frac{\partial v}{\partial y}=\frac{\partial}{\partial x}\left\{\frac{1+\mu_r}{\mathrm{Re}}\left(\frac{\partial u}{\partial y}+\frac{\partial v}{\partial x}\right)\right\}+\frac{\partial}{\partial y}\left\{2\frac{1+\mu_r}{\mathrm{Re}}\left(\frac{\partial v}{\partial y}\right)-p\right\} \quad (8)$$

where $\mu_r=\mu_t/\mu_L=\chi^4/\left(1+\chi^3\right)$, u is the x-component of the pure carrier velocity and v is its y-component, χ is the Spalart Allmaras turbulence variable obtained by solving the transport equation:

$$\frac{\partial}{\partial x}(u\chi)+\frac{\partial}{\partial y}(v\chi)=\frac{\partial}{\partial x}\left(\frac{1}{Re}\frac{1+\chi}{\sigma}\frac{\partial\chi}{\partial x}\right)+\frac{\partial}{\partial y}\left(\frac{1}{Re}\frac{1+\chi}{\sigma}\frac{\partial\chi}{\partial y}\right) \quad (9)$$
$$+\frac{c_{b2}}{\sigma\mathrm{Re}}\left\{\left(\frac{\partial\chi}{\partial x}\right)^2+\left(\frac{\partial\chi}{\partial y}\right)^2\right\}+f_{r1}c_{b1}\tilde{S}\chi-\frac{1}{\mathrm{Re}}\left(\frac{L}{d}\right)^2c_{w1}f_w\chi^2$$

where

$$\chi=\frac{\tilde{\upsilon}}{\upsilon};\quad \tilde{S}=S+\frac{1}{\mathrm{Re}}\left(\frac{L}{d}\right)^2\frac{\chi}{\kappa^2}f_{\upsilon 2};$$
$$f_{\upsilon 2}=1-\frac{\chi}{1+\chi f_{\upsilon 1}};\quad S=\sqrt{2S_{ij}S_{ij}} \quad (10)$$

S represents the magnitude of the strain rate (alternatively, magnitude of the vorticity can be taken), d is the distance closest to the wall.

$$f_w=g\left[\frac{1+c_{w3}^6}{g^6+c_{w3}^6}\right]^{\frac{1}{6}};\quad g=r+c_{w2}\left(r^6-r\right);\quad r=\frac{1}{\mathrm{Re}}\left(\frac{L}{d}\right)^2\frac{\chi}{\tilde{S}\kappa^2}. \quad (11)$$

The modification for the rotation and streamline curvature for Spalart-Allmaras one equation eddy viscosity model has been proposed in [13]. The production term $c_{b1}\tilde{S}\chi$ of the model is multiplied by the non-dimensional "rotation function" f_{r1},

$$f_{r1}\left(r^*,\tilde{r}\right)=\left(1+c_{r1}\right)\frac{2r^*}{1+r^*}\left\{1-c_{r3}\tan^{-1}\left(c_{r2}\tilde{r}\right)\right\}-c_{r1}, \quad (12)$$

$$r^*=S/\omega, \quad (13)$$

$$S^2=2S_{ij}S_{ij}=2u_x^2+2u_y^2+\left(u_y+v_x\right)^2, \quad (14)$$

$$\omega^2=2\omega_{ij}\omega_{ij}=\left(u_y-v_x\right)^2, \quad (15)$$

The additional model constants are $c_{r1}=1.0$, $c_{r2}=12$ and $c_{r3}=1.0$. $\tilde{r}=0$ for non-rotating flows. As discussed in [13], these values are open to refinement.

The x- and y-momentum equations for the solid species k are

$$\frac{\partial}{\partial x}\left(C_ku_ku_k\right)+\frac{\partial}{\partial y}\left(C_kv_ku_k\right)=-\frac{C_k}{S_k}\frac{\partial p}{\partial x}+C_kg_x$$
$$+\frac{3C_D}{4d_{eq,k}S_k}\left|\vec{u}_m-\vec{u}_k\right|\left(u_m-u_k\right)C_k\left(1-C\right)^{-1.65}$$
$$+\frac{1}{\mathrm{Re}}\left[\frac{\partial}{\partial x}C_k\left\{\begin{matrix}\frac{\upsilon_{kE}}{\upsilon_L}\left(\frac{4}{3}\frac{\partial u_k}{\partial x}-\frac{2}{3}\frac{\partial v_k}{\partial y}\right)\\-\frac{\upsilon_{kt}}{\upsilon_L\tan\theta}\left(\frac{\partial u_k}{\partial y}+\frac{\partial v_k}{\partial x}\right)\end{matrix}\right\}+\left[\frac{\partial}{\partial y}C_k\frac{\upsilon_{kE}}{\upsilon_L}\left(\frac{\partial u_k}{\partial y}+\frac{\partial v_k}{\partial x}\right)\right]\right] \quad (16)$$

and

$$\frac{\partial}{\partial x}\left(C_ku_kv_k\right)+\frac{\partial}{\partial y}\left(C_kv_kv_k\right)=-\frac{C_k}{S_k}\frac{\partial p}{\partial y}+C_kg_y$$
$$+\frac{3C_D}{4d_{eq,k}S_k}\left|\vec{u}_m-\vec{u}_k\right|\left(v_m-v_k\right)C_k\left(1-C\right)^{-1.65}$$
$$+\frac{1}{\mathrm{Re}}\left[\frac{\partial}{\partial x}C_k\frac{\upsilon_{kE}}{\upsilon_L}\left(\frac{\partial u_k}{\partial y}+\frac{\partial v_k}{\partial x}\right)\right]$$
$$+\frac{1}{\mathrm{Re}}\left[\frac{\partial}{\partial y}C_k\left\{\frac{\upsilon_{kE}}{\upsilon_L}\left(\frac{4}{3}\frac{\partial v_k}{\partial y}-\frac{2}{3}\frac{\partial u_k}{\partial x}\right)-\frac{\upsilon_{kt}}{\upsilon_L\tan\theta}\left(\frac{\partial u_k}{\partial y}+\frac{\partial v_k}{\partial x}\right)\right\}\right], \quad (17)$$

where $\upsilon_{kE}=\upsilon_k+\upsilon_{kt}$ is the effective viscosity of species 'k', $S_S=\rho_S/\rho_L$ is the relative density of solid, C_D is the drag coefficient, $\tan\theta$ is the dynamic friction coefficient [8], g_x and g_y are the components of gravitational acceleration, and $d_{eq,k}$ is the equivalent particle diameter of the k^{th} particle species after taking the shape factor (due to non-spherical shape) into account. The drag coefficent C_D (drag coefficient) is defined in terms of $d_{eq,k}$ and is given as

$$C_{Dk}=\begin{cases}\frac{24}{Re_p^k}\left[1+0.15\left(Re_p^k\right)^{0.687}\right] & \text{for } Re_p^k\le 1000\\ 0.44 & \text{for } Re_p^k>1000.\end{cases} \quad (18)$$

$$\mathrm{Re}_p^k=\frac{\rho_m d_{eq,k}\left|\vec{u}_m-\vec{u}_k\right|}{\mu_m'}. \quad (19)$$

where Re_p^k is the particle Reynolds number based on the equivalent particle diameter and the mixture viscosity and μ_m' is an apparent eddy viscosity experienced by the particles in the slurry mixture [17].

Reynolds averaging of the volume-averaged species continuity equation renders the classical convection-diffusion equation for species concentration as

$$\frac{\partial}{\partial x}\left(C_ku_k\right)+\frac{\partial}{\partial y}\left(C_kv_k\right)=\frac{\partial}{\partial x}\varepsilon_{kx}\frac{\partial C_k}{\partial x}+\frac{\partial}{\partial y}\varepsilon_{ky}\frac{\partial C_k}{\partial y} \quad (20)$$

The particle diffusivities ε_{kx} and ε_{ky} are computed in the same manner as done by Pagalthivarthi et al. [8].

B. Boundary Conditions

Boundary conditions are specified along the casing inlet, walls and the exit (in non-dimensional form) as follows:

Casing Inlet:

$$u_{k\_rad} = u_{m\_rad} = u_{l\_rad} = \frac{Q}{2\pi R_2 b};\ u_{k\_\tan} = u_{m\_\tan} = u_{l\_\tan} = \frac{gH}{\eta U_0};$$

$$C_k = C_{k,avg};\ \upsilon_t = C_\mu^{0.25}\sqrt{\frac{3}{2}}U_0 T_i L;\ L = 0.14R_2; \quad (21\text{ a-e})$$

where $u_{l\_rad}, u_{m\_rad}, u_{k\_rad}$ is the radial velocity of the carrier, mixture and k^{th} species velocity issuing from the impeller outer diameter, Q is the volumetric flow rate of the mixture, R_2 is the impeller outer radius, and b is the impeller passage width at impeller exit. The tangential velocity of the carrier $u_{l\_\tan}$, mixture $u_{m\_\tan}$ and k^{th} species $u_{k\_\tan}$ is defined based on the generated head, the pump efficiency, and the tip speed U_0 of the impeller, $C_{k,avg}$ is the average inlet concentration of the k^{th} species, L is the length scale, T_i is the turbulence intensity, υ_t is the kinematic eddy viscosity of the pure carrier flow, and $C_\mu = 0.09$ is a turbulence model constant. For illustration purposes, the velocities of all components of the mixture are assumed equal. In practice, the velocity of the mixture and that of each species at the casing inlet may differ. If this information is available, then it can be used in the specification of the boundary conditions.

Casing Walls:

Walls are assumed to be impermeable. Spalding wall functions [18] are applied as follows:

$$y^+ = u^+ + \exp(-\kappa b)\left[\begin{array}{l}\exp(\kappa u^+) - 1 - (\kappa u^+) \\ -(\kappa u^+)^2/2 - (\kappa u^+)^3/6\end{array}\right] \quad (22)$$

with $y^+ = \frac{y u_\tau}{\upsilon}$; $u^+ = \frac{u}{u_\tau}$; $\kappa = 0.41$ and $b = 5.0$. Here y is the distance from the wall, υ is the laminar viscosity of the flow component, and κ and b are empirical constants. Equation (22) is applied with the appropriate viscosity for each of the flow components as well as the mixture. The eddy viscosity at the wall (required by the Spalart-Allmaras model) is derived from the wall functions as

$$\upsilon_{tw} = \kappa u_\tau y_w \quad (23)$$

where the subscript w stands for the wall.

The gradient normal to the wall of the concentration of each species is assumed to vanish. Since the eddy viscosity approaches zero close enough to the wall, the zero normal gradient condition in stipulates a null mass flux normal to the wall. In other words, the walls are impermeable to all species of the mixture.

Casing Exit:

The gradients of all the variables (except pressure) in the direction normal to the discharge surface are assumed to be zero. In solving the least squares finite element equation for the pressure field, the pressure at the discharge exit is arbitrarily specified to be zero.

III. Numerical Algorithm

Fig. 2 summarizes the overall numerical algorithm. A sequential approach is used to solve the system of partial differential equations governing the carrier flow, the mixture flow and the individual particulate species momentum and mass continuity. Four-node finite elements are used for all field variables. First, the pure carrier flow field is computed with a reasonable initial guess (possibly generated using the potential function approach of [3]). The *x*- and *y*- momentum equations are rendered into weak form by streamline upwind Petrov-Galerkin (SUPG) formulation [14]. Pressure is handled via penalty formulation [19]. The eddy viscosity appearing in the momentum equations is computed from the Spalart-Allmaras equation. The discretized form of momentum equations is solved by combined Newton's iteration for an assumed eddy viscosity field. This is alternated with a Newton's iteration for solving the discretized form of the Spallart-Allmaras equation. Once the flow field is determined, pressure is computed by a least squares finite element method [19]. Following earlier studies [8], [10], the eddy viscosity field for the pure carrier phase (μ_t) is modified to account for the presence of particles to determine the eddy viscosity field (μ_{mt}) of the mixture and the eddy viscosity field (μ_{st}) of the solids.

The mixture flow field (u_m, v_m) is also computed using Newton's iteration applied to a SUPG penalty finite element formulation of the mixture momentum equations. The mixture pressure (p) is again computed by a least squares finite element computation. This is followed by a simultaneous Newton's solution of the SUPG finite element formulation of the *x*- and *y*- momentum equations of each individual species. This is then followed by the computation of the concentration field of each species governed by a SUPG discretized form of the convection-diffusion equation. Newton's iteration is also employed for the concentration of each species. The equation for mixture pressure (derived by least squares application to the mixture momentum equations) is linear in *p*, and hence it is solved without iteration. Pressure is assumed to be equal to that of the mixture for all solids species.

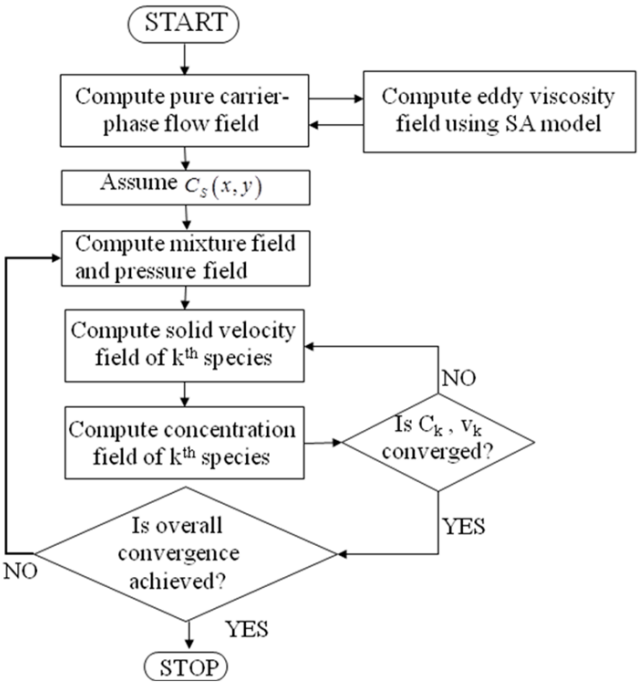

Fig. 2 Flow chart representing the numerical algorithm

All systems of algebraic equations are solved using PARDISO (linear solver in INTEL® MKL library) solver. All inner and outer iterations are carried out until the infinity norms of the correction vectors (New values – old values) of all field variables reach values less than 10^{-6}. In the overall iteration as well as in the inner iterations, suitable under-relaxation is used when necessary for convergence.

IV. Results and Discussion

Results for multi-size slurry flow through pump casings are not available in the published open literature. However, extensive favorable comparisons of the trends of the computed and experimental results [20] have been reported for multi-size slurry flow through two-dimensional channels [8], [10]. As the computational methodology used in these studies is essentially similar to that of the present study, the favorable match with experiments lends confidence to the present computations.

For the present study, a GIW slurry pump casing is used in all computations. The pump operating conditions at its best efficiency point (BEP) are shown in Table I. The operating head, pump efficiency and the flow rate determine the inlet flow velocity conditions at the casing inlet. Table II shows the important physical properties and pump parameters. Fig. 1 shows a typical two dimensional pump casing mesh. Gravity is acting in negative *y*-direction. Fig. 1 also shows the cross-sections along which the results are presented. The inlet concentration of the solids in the slurry is 30% by volume. Table III shows the particle size distribution (referred in the sequel as PSD) of the slurry. Solids are classified into six size classes with the particle diameter and inlet concentration of each size class as shown in Table III.

TABLE I
Pump Operating Conditions

Pump diameter	0.4572 m
Width of the impeller	0.172 m
Flow rate	366.68 liter/s
Operating head	20.39 m
Pump efficiency	72.6%
Turbulence intensity at casing inlet	7%

TABLE II
Values of Physical Quantities and Modeled Constants

ρ_L	1000 kg/m^3
μ_L	0.001 $N\text{-}s/m^2$
ρ_S	2820 kg/m^3
κ	0.4
E	9.8
$\tan\theta$	1.0
C_{pack} (packing concentration)	0.6
K_s (shape factor)	0.26 (for sand)

A. Mesh Independence Studies

To establish reasonable mesh independence of the solution, multi-size particulate flow simulations are performed on three different mesh sizes: (a) 5887 nodes, 5640 elements (b) 8594 nodes, 8300 elements (c) 12783 nodes, 12420 elements. The overall computation times for the three meshes are 12 minutes, 18 minutes and 39 minutes, respectively.

Fig. 3 shows the distribution of the total local concentration along the casing wall for the three meshes. The general trends for the three meshes are similar, and the solutions are close enough, especially for the two finer meshes. Fig. 4 shows the variation of the total concentration along different cross-sections. Apart from a slight difference in the discharge region (Section VII), the concentration profiles predicted by the three meshes are practically identical. The mass conservation for the pure carrier phase and the mixture velocity is well satisfied for all the three mesh sizes. The percentage difference between the total mass flow rate at the discharge and inlet is (for both pure carrier and the mixture) less than 0.1% for all the three meshes. For each of the individual species, the mass conservation is satisfied to within 0.5% for all three meshes, with finer meshes yielding superior conservation. Based on these results, the mesh consisting of 8300 elements is chosen for the subsequent simulations.

B. Insight into Multi-size Particulate Flow Features

Apart from showing the consistency of results with mesh refinement, Fig. 3 also gives important insight into the flow phenomena. There is a high local concentration peak at the stagnation point (point B) in the tongue region. The solids velocity is normal to the casing wall surface at and adjacent to the stagnation point, thus leading to a local accumulation of solids. Moving away from the stagnation point (towards point C), the velocity vectors become quickly parallel to the casing surface. In addition, the magnitude of the velocity increases in the throat region due to smaller cross-section area. Thus, the particles are transported along the casing surface quickly,

leading to a sharp decline in the concentration in the neighborhood of the stagnation point.

Further along in the belly region along the casing wall, traversing through points C, D, E, F, the concentration gently increases. The centrifugal action on the solid particles causes the particles to be pushed towards the casing wall. Of course, for a different set of off-design flow conditions, the concentration variation along the casing could be different.

At the entrance of the discharge region (i.e. points B and G) there is a complex interaction due to the change of cross-sectional area (the flow area increases after point F), the flow vectors pointing upward (as shown by streamlines in Fig. 5 (a)) in the discharge region. The concentration fluctuations in the region F to G are due to the effect of the stagnation point on the flow being communicated to the neighborhood, especially across the line B-G. In the discharge region (from point G to H), the concentration gradually decreases due to turbulent mixing as well as a reduction in the centrifugal action on the solid particles (due to straightening of the particle trajectory). The concentration eventually drops from point G to point H. Note that the concentration along the exit plane AH is in general higher than the average input concentration. This is necessitated to preserve overall conservation of mass flow rate.

Fig. 5 (a) shows the mixture velocity vectors and the streamlines in the flow field. A zoom-in view is provided near the tongue region. The tongue (cut-water) divides the flow into two parts and there is a stagnation region. The flow area decreases above the tongue, leading to high circumferential velocities in that local region. In the stagnation region, the velocity is nearly perpendicular to the casing surface. The velocity becomes increasingly tangential to the casing surface, right next to the stagnation region.

TABLE III
SLURRY DETAILS (PSD)

Species	Particle diameter (microns)	Volumetric concentration
1	750	1.7%
2	500	6.14%
3	250	10.23%
4	150	6.82%
5	100	3.41%
6	50	1.7%

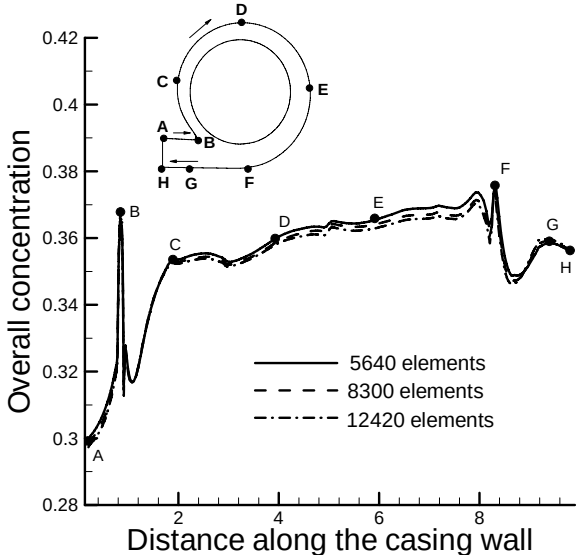

Fig. 3 Concentration along the casing periphery

Fig. 5 (b) shows the mixture pressure distribution. As anticipated, mixture pressure is highest near the tongue region at the stagnation point. The pressure increases in the radial direction from the casing inlet (*i.e.* impeller exit) to the casing wall due to centrifugal effect.

Fig. 6 shows the overall concentration contours. In the curved regions, the concentration increases moving out radially from the impeller exit towards the casing wall due to the particles being pushed outwards by centrifugal effect. As explained in the foregoing, there is a region of high local concentration at the stagnation point. The concentration tends to smear out a little in the discharge region of the casing.

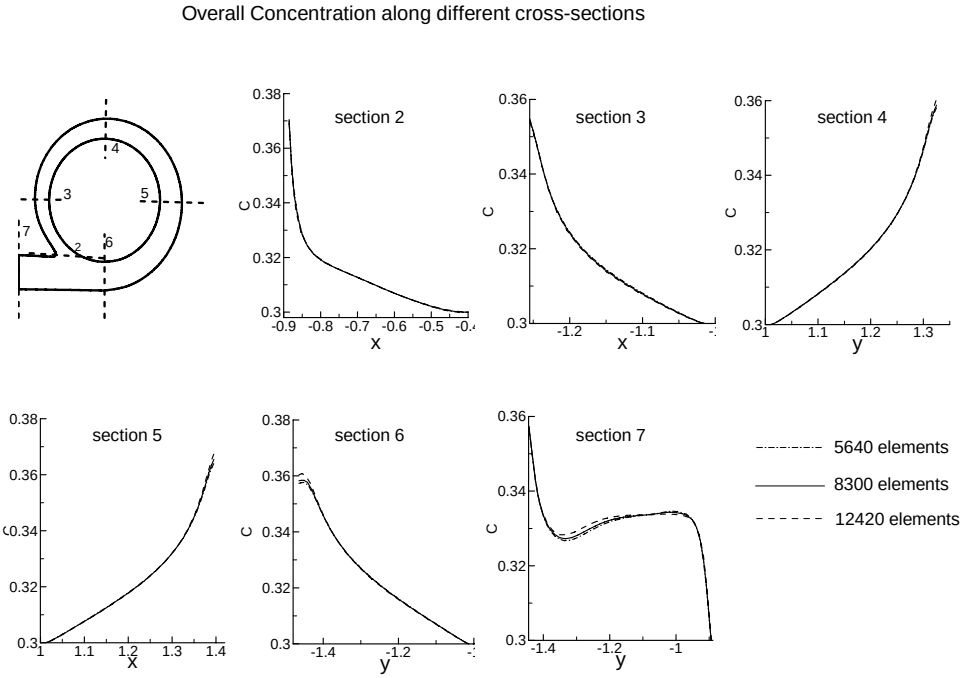

Fig. 4 Concentration profiles along the different cross-sections for three different meshes

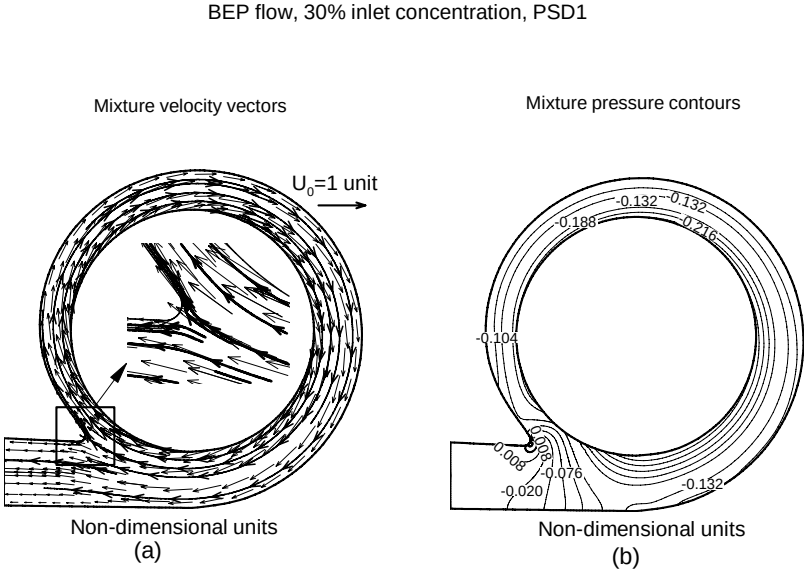

Fig. 5 (a) Mixture velocity vectors and streamlines (b) Mixture pressure contours for slurry in Table III

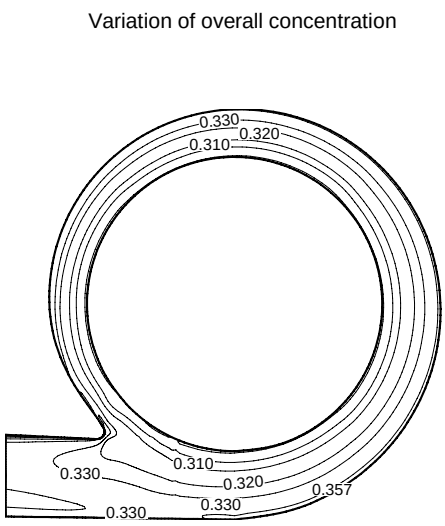

Fig. 6 Overall concentration contours

Fig. 7 shows the individual concentration variation of all the particle sizes along the casing wall. Similar trends are observed as in the case of overall concentration variation along the casing wall. It is to be noted that the larger size particles (1, 2 and 3) exhibit a significant increase in concentration along the casing wall. Larger particles experience greater centrifugal action, causing the particles to move closer to the wall. In the case of the smaller diameter particle (particle 6), the concentration variation is so small that it appears as a flat straight line.

Fig. 8 shows the individual concentration profiles of all the particle sizes along the different cross-sections. Along the cross-sections 2-6, the concentration increases radially from the casing inlet (*i.e.*, the impeller exit) to the casing wall. Along cross-section 7 the variation of concentration upon entry into the discharge is shown. Gravity also plays a role in causing the higher concentration on the lower side of the discharge. Gravity plays a reduced role in the concentration distribution in other cross sections. As explained before, the concentration gradients are higher for larger size particles and lower for the smaller size particles. A clear boundary-layer effect is seen near the casing walls.

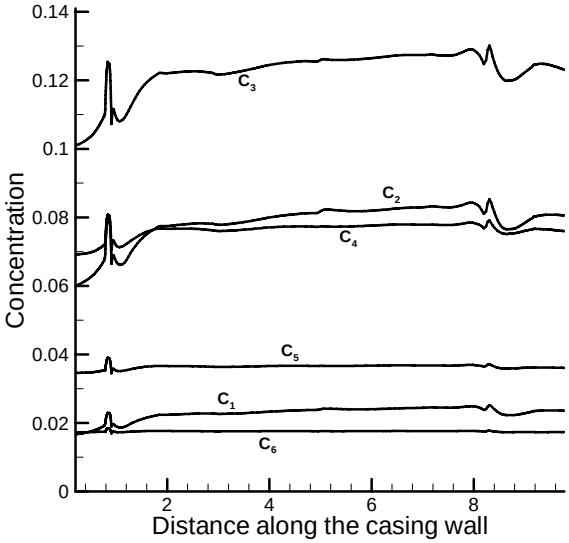

Fig. 7 Concentration variations for all the particle size classes along the casing wall

In Fig. 9, a comparison is made between simulations of multi-size particles and mono-size particles using (1) the weighted mean diameter of the size distribution (278 microns) and (2) the D50 particle size (180 microns). The overall concentration distribution along the casing wall is shown. It is observed that the mono-size particle simulation based on weighted average diameter over-predicts the concentration along the casing wall and the D50 particle size simulation under-predicts the concentration profiles. Clearly, the choice of D50 particle size is not a good representative of the PSD, given the fact that the D50 particle size does not contain information about the largest size particles and the smallest size particles. The concentration field is a strong function of the particle diameter. Hence the simulations based on D50 particle size can significantly deviate from the multi-size particulate flow simulation. The weighted average diameter could be a good representative of the PSD. However, the results show that the concentration field is over-predicted as compared to the multi-size flow simulations. The reason for this is explored in detail in section C where the effect of PSD on the flow field is discussed.

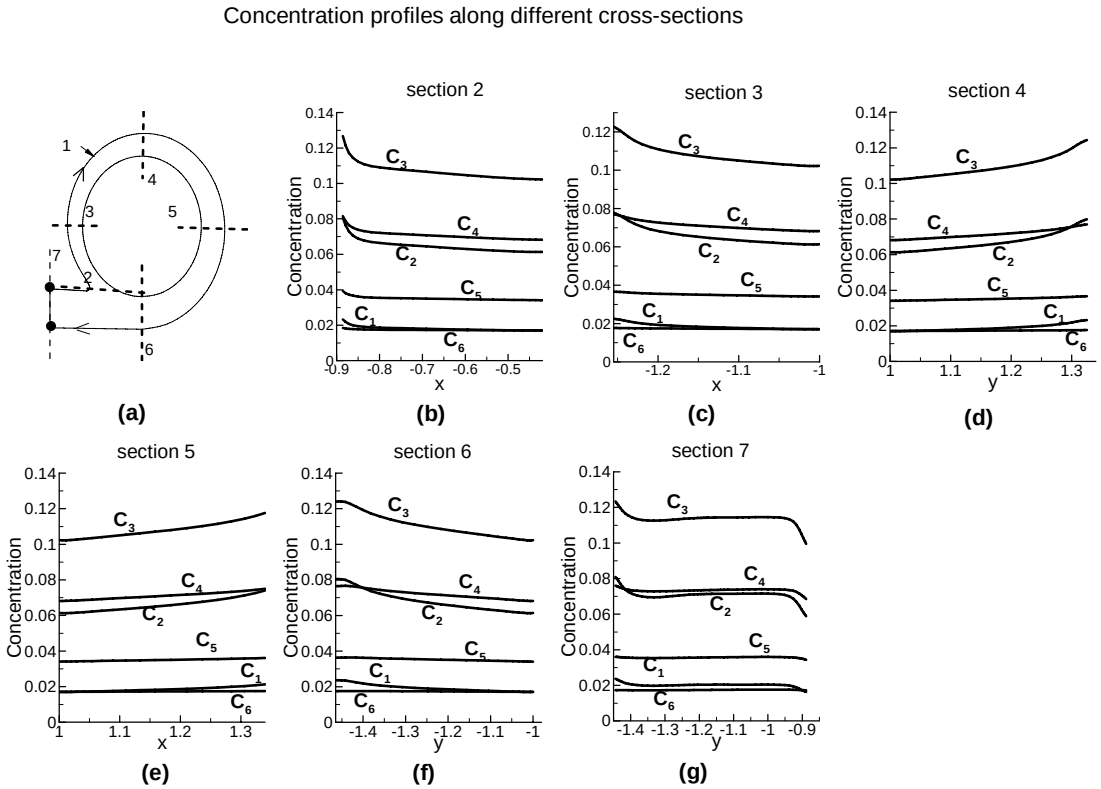

Fig. 8 Concentration profiles of all the particle size classes along cross-sections 1-7

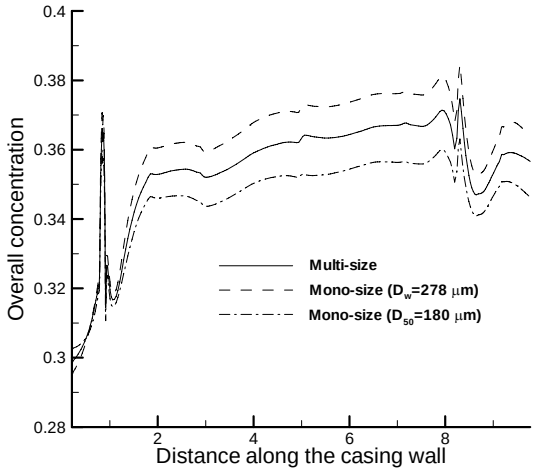

Fig. 9 Comparison of multi-size and mono-size simulations

C. Parametric Study

Parametric study is conducted to study the effect of different operating flow conditions and different inlet concentrations on the concentration distribution.

Effect of Flow Conditions

Three different flow conditions are used: (a) 100% BEP flow (b) 70% BEP flow and (c) 120% BEP flow. Fig. 10 shows the concentration distribution along the casing wall for the three flow conditions. The trends in the variation of concentration distribution for 70% BEP flow conditions, 100% BEP flow conditions and 120% BEP flow conditions remains similar. Flow rate has less significant effect on the concentration field. The overall concentration prediction along the casing wall is quite similar for all the three flow rates except within the discharge region. In the discharge region, the concentration of particles at the casing wall is larger for the 70% BEP flow rate as compared to the other two cases. First of all, for the less-than-BEP flow rate, there is substantial recirculation around in the casing, entraining some portion of particles with the recirculating flow. Second, the flow rate effects the eddy viscosity distribution inside the casing. As the flow rate increases, the eddy viscosity is higher, leading to a more rapid mixing. This in turn leads to a reduction in the concentration gradients, especially in the discharge region where the centrifugal effect quickly diminishes. Fig. 11 shows the concentration distribution along the different cross-sections. Fig. 11 (g) clearly shows that the concentration at the 6 O' Clock section is the highest (around 0.375) for the 70% BEP flow and lowest for the 120% BEP flow (around 0.345).

Fig. 12 shows the non-dimensional solid shear stress distribution of particle size class 1 along the casing wall for different flow rates. Although the concentration distribution is not significantly affected by the flow rate, the solid shear stress is affected (both in magnitude and in the trend of variation) by the flow rate. For 70% BEP flow case, the shear stress along the casing wall decreases (after the initial peak value at the tongue) till the discharge section, whereas for the 120% BEP flow case, the shear stress distribution increases along the casing wall. Similar trends are observed (not shown) for all the particle sizes. Since the shear of particles

significantly affects the erosion process, this would affect the trends in the wear rate distribution along the casing wall.

Fig. 13 shows the variation of frictional power ($c_k V_k \tau_k$) of particle size class 1 along the casing wall. Here, c_k is the concentration of the particle '*k*', V_k is the tangential velocity of the particle at the wall and τ_k is the shear stress of the particle. Frictional power is an indicator of the sliding wear rate along the walls. Fig. 13 shows a similar trend as in the case of solid shear stress distribution shown in Fig. 12.

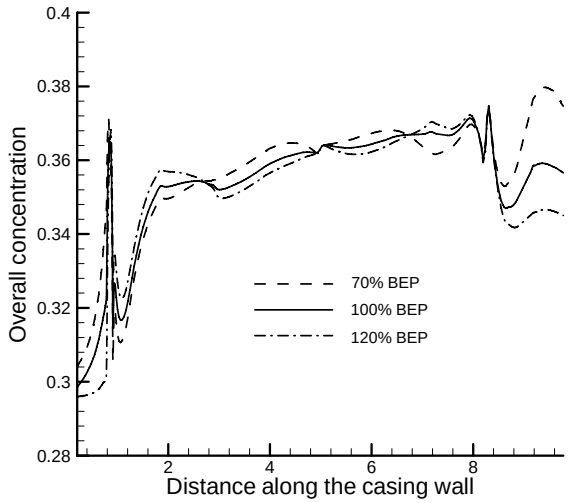

Fig. 10 Effect of flow rate on concentration along the casing wall

Effect of Particle inlet concentration

Figs. 14 and 15 show the effects of varying the inlet concentration (20-40% by volume). Once again, concentration distribution along the casing periphery and the concentration profiles at sections 1-7 are shown. The trends are quite similar for all the chosen inlet concentrations. All the cases have local peak concentration at the tongue. The concentration increase at the discharge section from point A to H is 0.2 to 0.279 for 20% inlet concentration case, 0.298 to 0.356 for the 30% inlet concentration case and 0.396 to 0.428 for the 40% inlet concentration case. The percentage increase is higher for the 20% inlet concentration case and lower for the 40% inlet concentration case. As the inlet concentration increases, particle-particle interactions increase. Thus with increasing inlet concentration, the concentration distribution tends to even out more. Moreover, the centrifugal action on the particles tends to be thwarted (hindered) by the presence of other particles.

Effect of Particle size distribution

In order to isolate the effect of particle size distribution (PSD), slurries with two particle size classes are chosen. Table IV shows the selection of three PSD's each consisting of only two particle sizes but all the three PSD's have the same weighted average diameter of 278 microns and the same overall concentration of 30%. PSD1 has a smaller range of particle diameter distribution and PSD3 has a larger range of particle diameter distribution.

TABLE IV
SLURRY DETAILS FOR THREE DIFFERENT PSD'S

Species	Particle Diameter (microns)	Concentration
PSD1		
1	300	23.53%
2	200	6.47%
PSD2		
1	400	15.41%
2	150	14.59%
PSD3		
1	500	13.38%
2	100	16.62%

(All PSDs have the same weighted mean diameter of 278 μm)

Fig. 16 shows that the concentration along the casing wall is consistently higher for PSD1 and lower for PSD3. In addition, the concentration prediction is higher for the mono-size particle simulation as compared to the other PSD's. This observation can be explained as follows. The weighted diameter of all the PSD's is the same. As the individual sizes of PSD deviates from the weighted diameter, the larger particles experience less drag and the smaller particles experience more drag. However, the functional dependence of the drag force on the particle diameter is non-linear (see (18)). The increase in drag force on the smaller particles is not compensated by the decrease in drag force on the larger particles. In other words, the magnitude of the increase in drag force on smaller particles is larger as compared to the magnitude of decrease in drag force on the larger particles. Correspondingly, the decrease in concentration gradient for the smaller size particles is larger than the increase in concentration gradient for the larger size particles. This leads to a decrease in the overall concentration along the casing wall as compared to the mono-size particles of weighted average diameter.

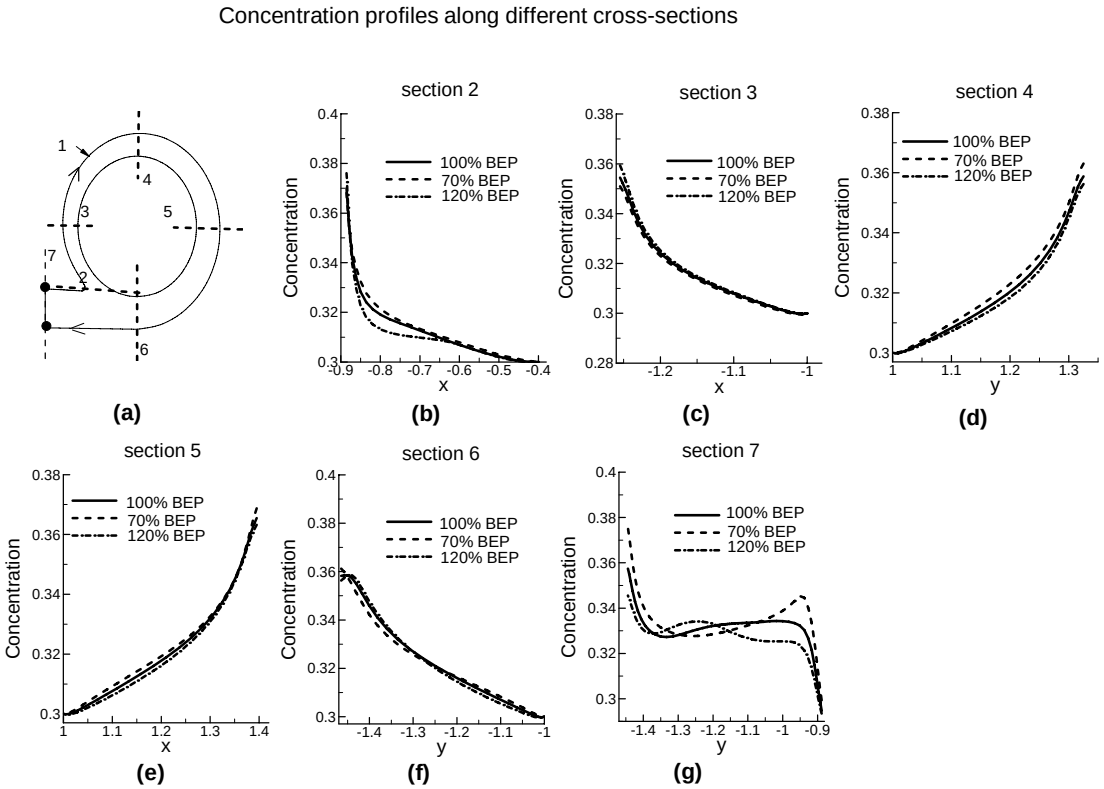

Fig. 11 Overall concentration profiles for different flow conditions along cross-sections 2-7

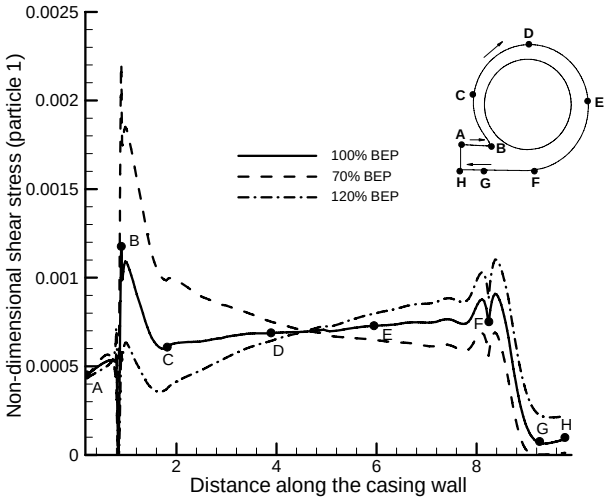

Fig. 12 Solid shear stress (particle 1) variation for different flow conditions

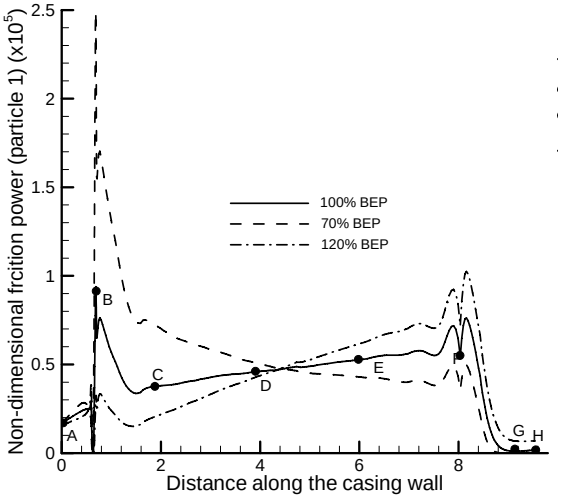

Fig. 13 Frictional power (particle 1) variation for different flow conditions

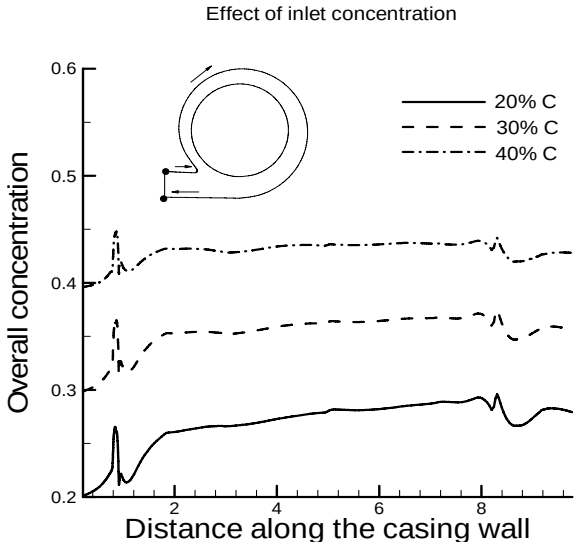

Fig. 14 Effect of inlet concentration on overall concentration along casing wall

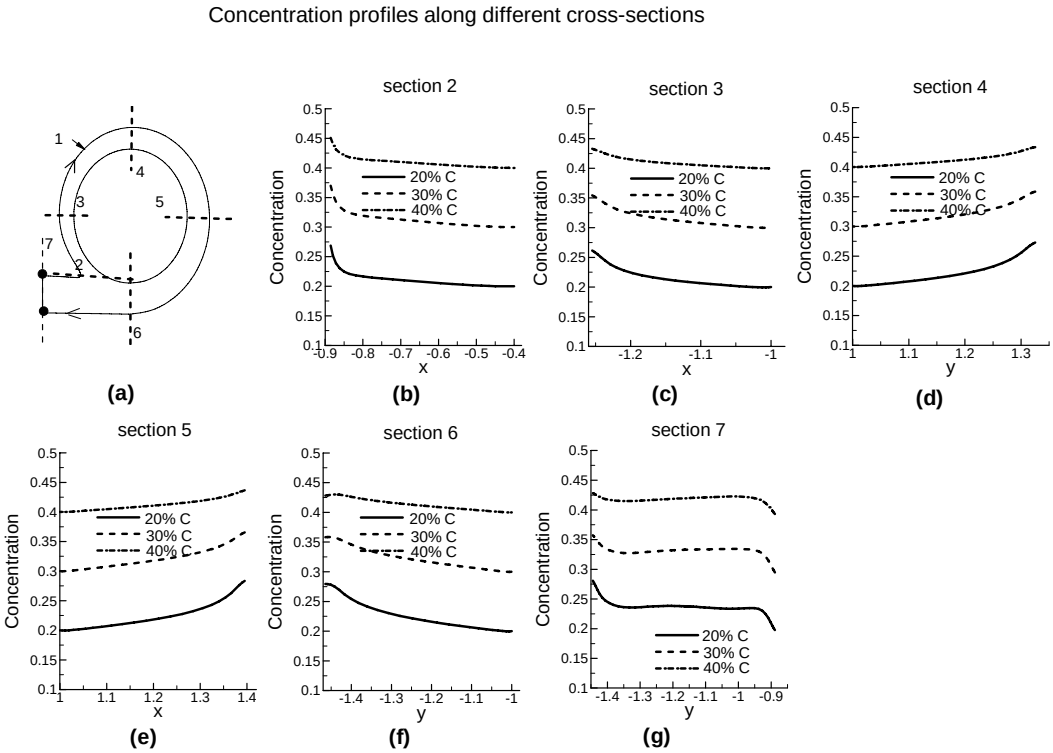

Fig. 15 Overall concentration profiles for different inlet concentrations along cross-sections 2-7

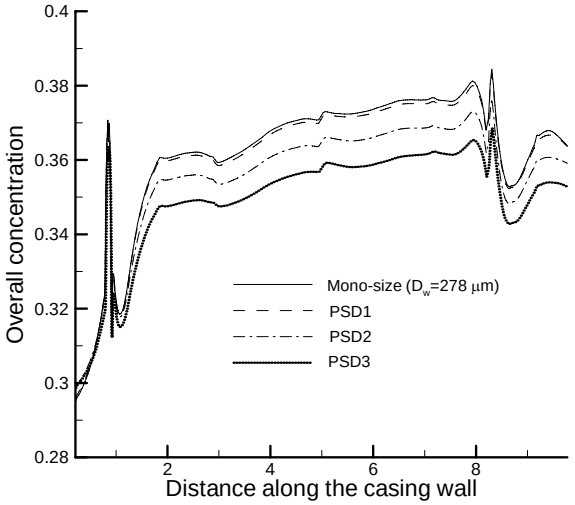

Fig. 16 Effect of PSD on concentration along casing wall

If the PSD consists of individual particle sizes which are closer to the weighted average diameter, then the concentration prediction will be closer to the results predicted by mono-size particle simulation based on the weighted mean diameter. As the PSD deviates from the weighted average diameter of the PSD (range of the particle sizes is large), the overall concentration prediction along the casing wall will decrease. This further leads to the conclusion that the mono-size particle simulation with the weighted mean diameter will predict larger concentration as compared to any other PSD with the same weighted average diameter. Hence Fig. 9 shows the over prediction of concentration for the mono-size slurry simulation based on the weighted average diameter as compared to the multi size particle simulation.

V. Conclusions

Multi-size particulate flow inside a two-dimensional pump casing is modeled using SUPG penalty finite element method. The slurry particle size distribution is represented as different size classes, each with its characteristic diameter. Results show near the stagnation point (in the tongue area), there is a local high concentration of solid. In general, the centrifugal action forces the particles to move towards the casing wall leading to a higher concentration near the casing wall. In the discharge section, the centrifugal action is dissipated leading to a gradual smearing out of the concentration distribution in the discharge section. Comparison is made for the multi-size simulations with the mono-size simulations using both weighted average diameter and D50 particle size diameter. It is shown that mono-size particle simulations deviate from the multi-size particle simulations indicating the importance of multi-size particle simulations. For the range of parameters studied, the pump inlet flow rate only slightly affects the concentration distribution inside the casing. However, the particle shear stress and the friction power of the particles along the casing wall are significantly affected by the inlet flow rate. With increasing inlet particle concentration, the trends in the concentration variation are similar but the concentration gradients tend to decrease in general. It is also shown that more the individual size distributions in the PSD deviate from the weighted average diameter of the PSD, the concentration along the casing wall will decrease.

Acknowledgment

The authors gratefully acknowledge the complete support provided by GIW Industries, Inc. for carrying out this research.

References

[1] M.C. Roco and G. R. Addie "Analytical Model and Experimental Study on Slurry Flow and Erosion in Pump Casings," *Slurry Transportation*, STA, vol. 8, pp. 263-271, 1983.

[2] M.C. Roco, and C. A. Shook, "Computational Model for Coal Slurry Pipelines with Heterogeneous Size Distribution," *Powder Technology*, vol. 39, pp. 159-176, 1984.

[3] G.R. Addie, and K. V. Pagalthivarthi, "Prediction of Dredge Pump Shell Wear," in: *Proc. WODCON XII, 12th World Dredging Conference*, World Organization of Dredging Associations, Arlington, VA, pp. 481-504, 1989.

[4] K.V. Pagalthivarthi, P.V. Desai, and G. R. Addie, "Particulate Motion and Concentration fields in Centrifugal Pumps," *Particulate Science and Technology*, vol. 8, pp. 77-96, 1990.

[5] R.J. Visintainer, G. R. Addie, and K. V. Pagalthivarthi, "Prediction of Centrifugal Slurry Pump Wear," *International Conf. on Pump and system*, Beijing, China, May 19-21, 1992.

[6] G.R. Addie, K. V. Pagalthivarthi, and J. R. Kadambi, "PIV and Finite Element Comparisons of Particles inside a Slurry Pump Casing," in *Proc. Int. Conf. on Hydrotransport 16*, Santiago, Chile, pp. 547-559, 2004.

[7] J.S. Ravichandra, K. V. Pagalthivarthi, and S. Sanghi, "Finite Element Study of Multi-size Particulate Flow in Horizontal Pipe," *Progress in Computational Fluid Dynamics*, vol. 4, no. 6, pp. 299-308, 2004.

[8] K.V. Pagalthivarthi, J. S. Ravichandra, and S. Sanghi, "Multi-size Particulate Flow in Horizontal Ducts – Modeling and Validation," *Progress in Computational Fluid Dynamics*, vol. 5, no. 8, pp. 466-481, 2005.

[9] P.K. Gupta, and K.V. Pagalthivarthi, "Effect of Diffusive Stress, Lift and Virtual Mass Forces on Multi-size Particulate Flow through Rotating Channel," in: Dwivedy, S. K. and Maity, D., ed(s), *Proc. Int. Cong. Computational Mechanics and Simulation*, IIT Guwahati, India, December 8-10, 2006.

[10] P.K. Gupta, and K. V. Pagalthivarthi, "Finite Element Modelling and Simulation of Multi-Size Particulate Flow through Rotating Channel," *Prog. Comp. Fluid Dynamics*, vol. 7, pp. 247-260, 2007.

[11] K.V. Pagalthivarthi, and P. K. Gupta, "Prediction of Erosion Wear in Multi-size Particulate Flow through Rotating Channels," *Fluid Dynamics & Materials Processing*, vol. 5, no. 1, pp. 93-122, 2009.

[12] P.R. Spalart, and S. R. Allmaras, "A One-Equation Turbulence Model for Aerodynamic Flows," *La Recherche Aerospatiale*, vol. 1, pp. 5-21, 1994.

[13] M. L. Shur, M. K. Strelets, and A. K. Travin, "Turbulence Modeling in Rotating and Curved Channels: Assessing the Spalart-Shur Correction," *AIAA Journal*, vol. 38, no. 5, pp. 784-792, 2000.

[14] T.J.R. Hughes, and A. Brooks, "A Theoretical Framework for Petrov-Galerkin Methods with Discontinuous Weighting Functions: Application to the Streamline Upwind Procedure," *Finite Elements in Fluids*, Eds. R. H. Gallagher et. al., vol. 4, pp. 47-65, 1982.

[15] M.R. Davidson, "A Numerical Model of Liquid-Solid Flow in a Hydrocyclone with High Solids Fraction," *Numerical Methods in Multiphase Flows*, ASME, vol. 185, pp. 29-38, 1994.

[16] M. C. Roco, and N. Balakrishnan, "Multidimensional Flow Analysis of Solid-Liquid Mixtures," *J. Rheology*, vol. 29, pp. 431-456, 1985.

[17] S. L. Lee, "Particle drag in a dilute turbulent two-phase suspension flow," *International Journal of Multiphase flow*, vol. 13, no. 2, pp. 247-256, 1987.

[18] F.M. White, *Viscous Fluid Flow*, 2nd Ed. McGraw-Hill, NY, 1991.

[19] J. N. Reddy, and D. K. Gartling, *The finite element method*, CRC Press, 1994.

[20] D. R. Kaushal, V. Seshadri, and S. N. Singh, "Prediction of Concentration and Particle Size Distribution in the Flow of Multisized Particulate Slurry through Rectangular Duct," *Appl. Math. Modeling*, vol. 26, pp. 941-952, 2002.